Author/s:
Seibt, S;Zhang, H;Mudie, S;Förster, S;Mulvaney, P

Title:
Growth of Gold Nanorods: A SAXS Study

Date:
2021-09-16

Citation:
Seibt, S., Zhang, H., Mudie, S., Förster, S. & Mulvaney, P. (2021). Growth of Gold Nanorods: A SAXS Study. Journal of Physical Chemistry C, 125 (36), pp.19947-19960. https://doi.org/10.1021/acs.jpcc.1c06778.

Persistent Link:
https://hdl.handle.net/11343/344948

The Growth of Gold Nanorods - A SAXS Study

Susanne Seibt,[†,‡,¶] Heyou Zhang,[¶] Stephen Mudie,[†] Stephan Förster,[§] and Paul Mulvaney[*,¶]

†*SAXS / WAXS Beamline, Australian Synchrotron, ANSTO, 800 Blackburn Road, VIC 3168 Clayton, Australia.*

‡*Physical Chemistry I, University of Bayreuth, Universitätsstraße 30, 95448 Bayreuth, Germany*

¶*ARC Centre of Excellence in Exciton Science, School of Chemistry,The University of Melbourne, Parkville, VIC 3010, Australia*

§*JCNS-1/ICS-1, Forschungszentrum Jülich, 52428 Jülich, Germany*

E-mail: mulvaney@unimelb.edu.au

Abstract

Using simultaneous, *in situ* optical spectroscopy and time-resolved, small-angle X-ray scattering (SAXS), we have directly monitored the seeded growth of nearly monodisperse gold nanorods using hydroquinone as the reductant. Growth of the rods is much slower than with ascorbate ion allowing the rate of growth along both the longitudinal and transverse directions to be independently determined. The thickness of the stabilising CTAB layer (3.2 nm ± 0.3 nm) has also been extracted. We find that increasing the hydrogen tetrachloroaurate(III) concentration produces longer rods, while conversely increasing the hydroquinone concentration reduces the final aspect ratio. The final number of gold rods is smaller than the initial number of seed particles and decreases in the presence of larger concentrations of $HAuCl_4$. The SAXS data reveal an early transition from spherical morphology to an ellipsoidal one and then to spherically

capped cylinders. The growth curve exhibits at least three distinct regimes: an initial phase comprising spherical seed growth, followed by symmetry breaking and slow elongation. A third phase is marked by rapid rod growth and increases in the aspect ratio. This process is temporally well resolved from the initial symmetry breaking but typically occurs when the rods are around 6 nm in diameter using hydroquinone as the reductant. The results provide qualitative support for the "popcorn model" proposed by Edgar et al. (ACS Nano **2012**, *6*, 1116-1125.)

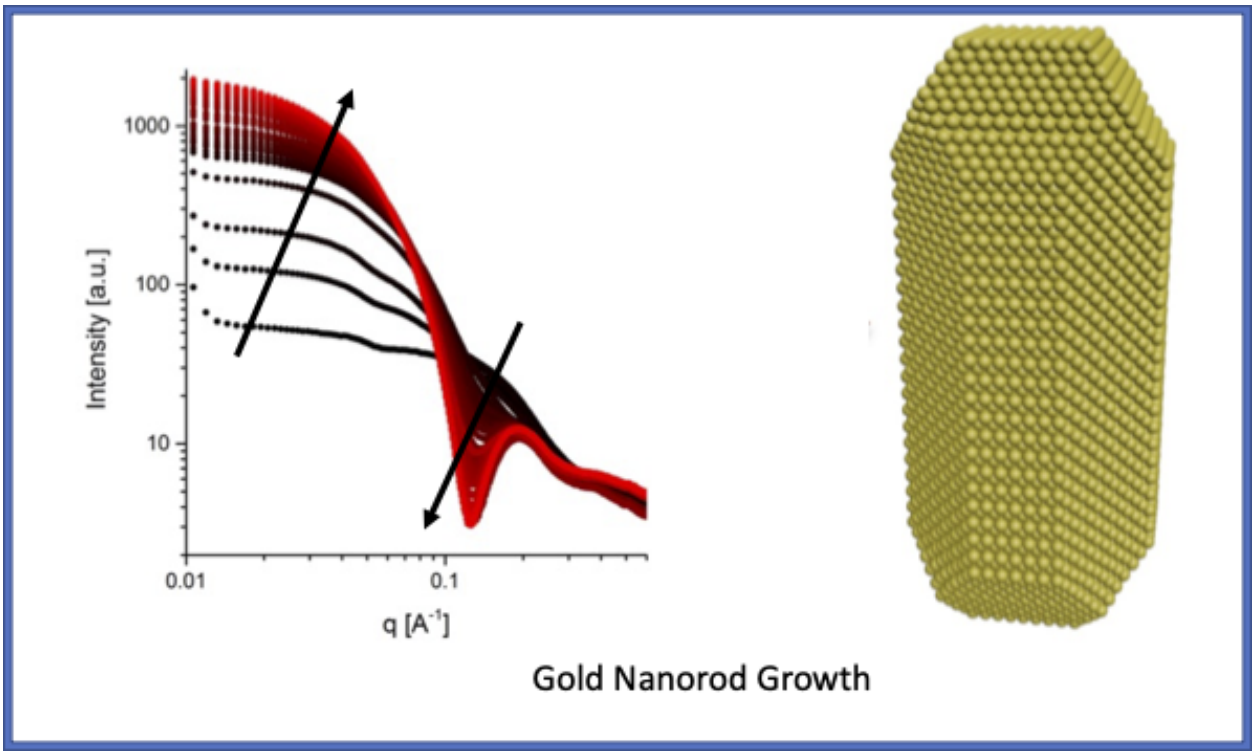

TOC graphic.

INTRODUCTION

Shape control of nanocrystals lies at the heart of self-assembly. Colloids of rod-like nanocrystals such as those of FeOOH or Al_2O_3 rods can exhibit rich phase behaviour, depending on the particle concentration and the particle aspect ratio. Consequently, there has been long standing interest in the role of crystal modifiers and inhibitors, which can alter the crystal morphology or control the aspect ratio and size of small particles. The synthesis of gold nanorods has garnered a lot of attention, following the discovery by Wang and colleagues that CTAB and $AgNO_3$ can induce rod formation in this system.[1] Rapid improvements in the synthesis has enabled the rods to be prepared at larger scale.[2,3]In addition to forming interesting colloid phases, these materials also exhibit very dramatic colour changes due to the presence of surface plasmon resonances. The energies of these resonance are strongly morphology dependent.

A key challenge is the measurement of the nanorod size as a function of time during the synthesis. Most researchers have used optical spectroscopy to monitor particle growth but it is impossible to unambiguously determine both the width and length of the growing particles from the optical spectrum of the gold nanorods alone.[2–4] Furthermore, as the spectra are both size and morphology-dependent, the spectral analysis is difficult, especially during the early growth phase when the surface plasmon resonances are typically weak and broad. Despite this, Sönnichsen and colleagues demonstrated that even the growth of a single nanorod can be studied using dark field spectroscopy.[5] An alternative approach is to use high resolution electron microscopy, which can provide direct insights into the symmetry breaking steps and a better understanding of the growth mechanism.[6–10] However, electron microscopy does not offer time resolved measurements since samples must be extracted and the number of particles examinable is only a small subset of the ensemble.

Nevertheless, these seminal electron microscopy studies have revealed that there is an

unusual, symmetry breaking event during particle synthesis and thereafter the nascent rods slowly elongate. However, basic questions remain unanswered. For example, it is unclear whether the facets grow at constant rates and whether silver ions influence just the symmetry breaking event or whether they continue to steer rod growth through the reaction.[11,12]

To answer these questions, one needs to be able to measure the length and width as a function of time. One approach is small-angle X-ray scattering (SAXS). SAXS measurements can in principle yield both the length and width of the rods. Several SAXS-based studies of spherical gold nanoparticle growth have been carried out. In pioneering studies, Polte et al. studied the growth of gold spheres with millisecond time resolution using a continuous flow system[13,14] combined with SAXS detection, while Hatakeyama et al. combined UV-vis, XANES and SAXS measurements to study ascorbic acid induced gold nanorod growth.[15,16] The main focus of the study by Hatakeyama was the role of different surfactants. These studies have shown that synchrotron X-ray scattering provides the necessary time resolution to study the growth kinetics of nanocrystals.[17,18] Other studies of metal nanocrystal growth using SAXS have been reported but to date,[19] SAXS has not been used to monitor shape changes during nucleation and growth.

Here we use time-resolved synchrotron-SAXS measurements to monitor the hydroquinone-based growth of gold nanorods. Hydroquinone is a weaker reductant than ascorbic acid and its use leads to slower growth such that the complete range of time scales from the early to late growth stages can be followed in detail using simultaneous synchrotron-SAXS and UV/Vis-spectroscopy. In addition, the use of hydroquinone leads to near quantitative conversion of the gold (III) ions into monodisperse gold nanorods.[20] This is a very efficient synthesis of gold nanorods without the need for subsequent purification steps which for the ascorbic acid route is routinely the case. Furthermore, the uniform conversion of spherical nanoparticles into nanorods allows tuning of the longitudinal surface plasmon resonance

(LSPR) peak beyond 1000 nm[21] and also enables independent determination of both the width and the length of the nanorods. A seedless version of this synthesis has also been reported by Li and colleagues.[22]

Our results demonstrate that synchrotron-SAXS is an ideal tool for exploring nanocrystal nucleation and growth. Our data support recent HRTEM studies on the symmetry breaking and rod growth process and are consistent with the concept of the "popcorn" model that has been proposed to explain some of the growth kinetics observed spectrophotometrically.[23,24]

METHODS

Hydrogen tetrachloroaurate (III) trihydrate ($HAuCl_4 \cdot 3H_2O$, $\geq 99.9\%$) was purchased from Alfa Aesar and used without further purification. Sodium borohydride ($NaBH_4$, $\geq 99.99\%$), silver(I) nitrate ($AgNO_3$, $\geq 99.9\%$), hexadecyltrimethylammonium bromide (CTAB, 96%) and hydroquinone (HQ, $\geq 99\%$) were purchased from Sigma-Aldrich and used without further purification. All solutions were freshly prepared using Millipore-filtered water.

Synthesis of CTAB-capped Au seeds.

5 mL of 0.50 mM aqueous $HAuCl_4$ solution and 5 mL of 0.20 M aqueous CTAB solution were mixed and stirred for 10 min at room temperature. Next, 600 μL of a freshly prepared 0.01 M $NaBH_4$ solution was added quickly under vigorous stirring. After 2 min, the stirring was stopped, and the seeds were aged for 1 h at room temperature.

Synthesis of monocrystalline Au nanorods.

To 2.5 mL of a 0.10 M aqueous CTAB solution, 12.5 μL of $HAuCl_4$ (0.1 M, 0.15 M, or 0.2 M) and 12.5 μL 0.1 M $AgNO_3$ solution were added and mixed until homogeneously dissolved. 125 μL of an aqueous HQ solution (0.2 M, 0.4 M, 0.6 M) was then added and the growth

solution gently mixed, leading to complete decolourisation. Finally, 100 μL of the 1h aged CTAB-capped Au seeds were added and mixed thoroughly for 30 seconds. The Au nanorods were then grown in the unstirred solution for 24 h at room temperature. Experiments were carried out at 22°C.

Characterisation.

UV-Vis spectra were recorded on an Agilent HP 8453 instrument in cuvettes with 1 cm path-length. TEM images were obtained with a LEO 922 OMEGA EFTEM with an acceleration voltage of 200 kV from Zeiss (Germany). Zero-loss filtered images were recorded using a bottom mounted Ultrascan 1000 (Gatan) CCD camera system. Gatan Digital Micrograph 3.9 for GMS 1.4 software was used for image acquisition. For the TEM analysis, 4 μL of the as-prepared solution was dried on a mesh copper grid with carbon foil. For size evaluation, the software ImageJ (version 1.44p, U.S. National Institute of Health) was used. 200 nanoparticles per sample were measured manually as well as using the ImageJ algorithm 'Measure_ROI.class'.

COMSOL Simulations.

The simulations were carried with the Radio Frequency (RF) module in 3D geometry. The geometry of the model used is shown in Figure S1. Figure S1a shows two main domains in the simulation. The outer layer in grey is the perfectly matched layer (PML) domain, while the inner body in blue is the physical domain, which contains a gold nanoparticle and surrounding environment. The size of the entire model is illustrated separately as both a "front view" and "top view" in figures S1b and S1c respectively. The geometry of the gold nanorod (Figure S1d) was a hemispherically capped cylindrical rod with input length (L) and width (W). The gold nanorod was located in the middle of the physical domain. The spectra were simulated across the wavelength range from 500 nm to 1100 nm with 5 nm steps. The refractive index of the surrounding environment was set as 1.33 and the complex refractive

indices of gold were taken from Johnson and Christy.[25] No mean free path corrections were included.

Kinetic experiment setup.

2.65 mL of the growth solution was prepared as described earlier in a vial and the seeds injected, followed by thorough mixing. The solution containing the growing nanoparticles was used to fill an air-tight Hamilton© syringe, connected via tubing to a 1 mm quartz capillary. The filled capillary was placed in a 3D-printed holder in the X-ray beam (shown in Figure 1). The solution was pumped through the capillary at a rate of 100 μL/h to ensure no beam damage during the growth phase of the nanorods. These kinetic experiments were carried out for all 9 combinations of $HAuCl_4$ and HQ concentrations and the total measuring time adjusted until no change in the measured SAXS curve could be observed. The time needed varied from one to seven hours.

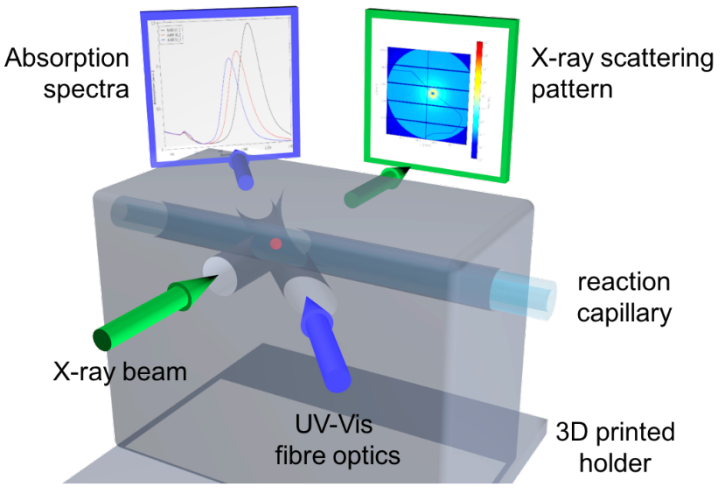

Figure 1: Drawing of the in-situ simultaneous SAXS/UV-Vis setup for measuring the growth kinetics of gold nanorods at the Australian Synchrotron. The quartz capillary had a diameter of 1.0 mm. Measurements were collected at ambient temperature. The X-ray beam size was about 250 μm x 25 μm, while the optic fibre used for spectroscopic data collection was focussed down to a waist of 400 μm.

SAXS and UV-vis Absorption Measurements.

Initial attempts to follow the reaction using a steady-state X-ray source yielded poor data and required long integration times. Hence, we turned to synchrotron based SAXS measurements, which reduced this integration time from $\sim$ 4 minutes down to $\sim$10 seconds.

SAXS experiments were performed on the SAXS/WAXS beamline at the Australian Synchrotron, Melbourne, Australia.[26] An energy of 11.5 keV was used with a sample to detector distance of 1.6 m, leading to a q-range of approximately 0.01 to 0.75 Å^{-1}. Two-dimensional SAXS patterns were acquired with a PILATUS2 1M detector and azimuthally averaged to yield the SAXS intensity I(q) profiles. An exposure time of 10 s was required for good counting statistics. A 50 s delay time between exposures produced a 1 minute sampling period. The shutter was closed between exposures to prevent sample damage through heterogeneous X-ray induced nucleation. For simultaneous *in situ* absorption measurements, an Ocean Optics UV-Vis spectrometer was used, which comprised a HR2000 detector (detection range 200 – 1100 nm) in combination with a DH-2000-BAL UV-Vis-NIR light source (deuterium

and halogen lamp, illumination range 215 – 2000 nm) and QP400-2-SR optical fibres (operating range 200 – 1100 nm). The optical fibres were mounted at a 45-degree angle to the capillary axis. All *in situ* measurements were background corrected using a capillary filled with 0.10 M CTAB solution. *In situ* here refers to synthesis in a capillary at the synchrotron SAXS beamline. As shown in the Supporting Information (Figure S2), we obtained consistent results when we compared the UV-vis spectra of gold rods made in a batch process.

RESULTS AND DISCUSSION

I. Electron microscopy

The gold nanorods were grown using the hydroquinone-based synthesis developed by Vigderman[20,21] and this led to nearly monodisperse gold nanorods with at least 95% gravimetric gold metal yield. Due to the low reactivity of hydroquinone, the growth of the nanorods took place over several hours, which rendered the reaction amenable to SAXS studies. The concentrations of $HAuCl_4$ and hydroquinone were systematically varied, while the concentration of $AgNO_3$ was held constant at 0.45 mM for all syntheses. The concentrations of $HAuCl_4$ in the gold rod solutions were 0.45 mM, 0.68 mM or 0.91 mM, while for hydroquinone the concentrations were 9.09 mM, 18.18 mM or 27.27 mM.

Typical TEM images of unpurified nanorod samples from *in situ* reactions in a capillary are shown in Figure 2. No purification was undertaken after reaction. The rods were simply allowed to sit overnight after synthesis at 15^{o}C which allowed excess CTAB to precipitate. TEM grids were prepared from a drop of the supernatant liquid. The mean particle dimensions are shown as well as the estimated standard deviations for three hydroquinone concentrations and three $HAuCl_4$ concentrations. Importantly, the experimental protocol yielded solutions containing almost exclusively nanorods and the polydispersity in both length and

width was typically around 3%. TEM showed no significant presence of small rods or spheres, except for sample S9, which contained about 10% spheres.Higher resolution images showed that the rods could be well approximated as spherically capped cylinders at longer times. There are two important trends that are immediately apparent from the TEM images. The first trend is that there was a strong increase in the final rod length with increasing concentrations of $HAuCl_4$, as well as a smaller increase in the rod width. The second observation is that there was a strong decrease in the final rod length with increasing hydroquinone concentration. The width also decreased slightly but the effect was not pronounced.

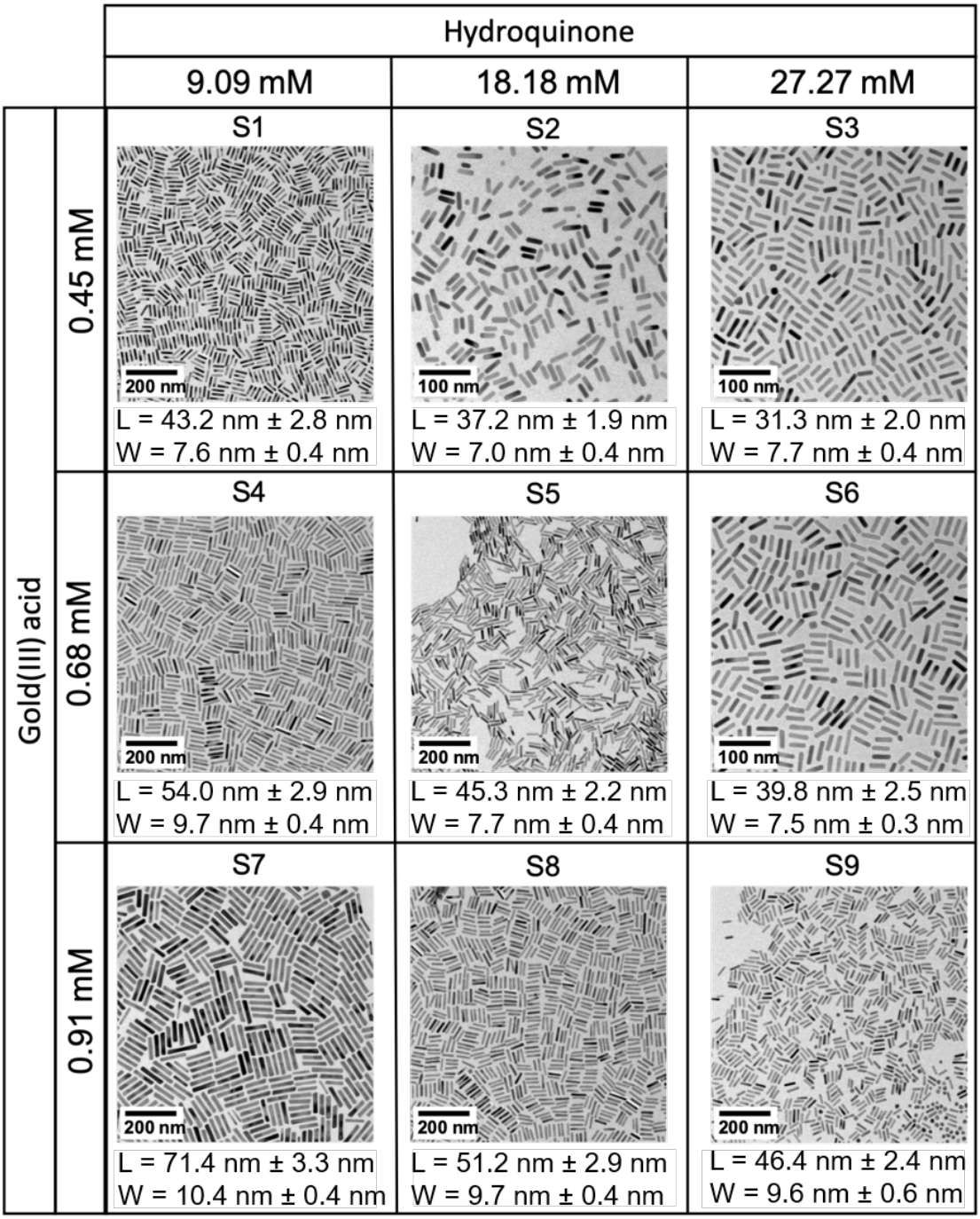

Figure 2: TEM images of the final gold nanorods from *in-situ* reactions and the corresponding sample dimensions. No post-synthesis purification was carried out and all the samples showed negligible concentrations of gold spheres. TEM samples were prepared on carbon coated grids and the images were collected at 200kV. 200 particles per sample were measured. [$AgNO_3$] = 0.45 mM for all syntheses.

II.SAXS analysis

The LSPR wavelength is sensitive to particle shape, hence one cannot determine growth rates or particle sizes from absorption spectroscopy. The extinction coefficient is dependent on absolute length, absolute width and also the endcap geometry.[27,28] However, SAXS can be used to obtain both length and width as a function of time, provided the particle shape is well-defined (compare Figure 3). The intensity of the scattered X-ray beam from a solution of particles is given as a function of the scattering vector, q, by:[29]

$$I(q) = V^2(\Delta\rho)^2 \int_0 [f(qr)]^2 n(r) S(qr) dr \tag{1}$$

Here, V is the total volume of scatterers and increases during the reaction, $\Delta\rho$ is the electron density, n(r) is the size distribution of the scatterers, f(qr) is the form factor and S(qr) is the structure factor. For a dilute samples S(qr) $\sim$ 1 and if the sample is close to monodisperse, n(r) $\sim$ 1. The form factor therefore determines the shape of the I(q) curve. In the Appendix we detail the explicit form factors used here. We have assumed three shapes: spherical, ellipsoidal and sphero-cylindrical. In addition, we include the formulae used for a core-shell particle with these three morphologies. At low q values, I(q) tends to a constant value proportional to the particle volume. The intermediate slope is characteristic of the shape; for example for spheres it decays as q^{-3} to q^{-4}, whereas for rods, it falls off as q^{-1}. To process the data, a background scattering spectrum from a solution of CTAB was used. Typical SAXS processing is illustrated in Figure S11, which also highlights the fitting process for both core and core-shell models.

Figure 3 shows four different scattering curves, collected at different times during synthesis S3 and the best fits to each set of data are shown for the three different morphologies. It is evident that only one morphology for each set of scattering data yields a satisfactory fit. During the early stages of the reaction, the spherical model yields the best fit, although the ellipsoidal geometry and the spherically capped cylinder geometry also cede reasonable

fits. However, the ellipsoidal fitting model includes an anisotropy factor (equal to the aspect ratio), which in these cases is close to one, so the particle can be considered spherical.When the data are fitted using a spherically capped cylinder, this results in the same radius as the spherical fit and with a length equal to double the radius (L = 2R), i.e. this model again cedes a spherical shape.

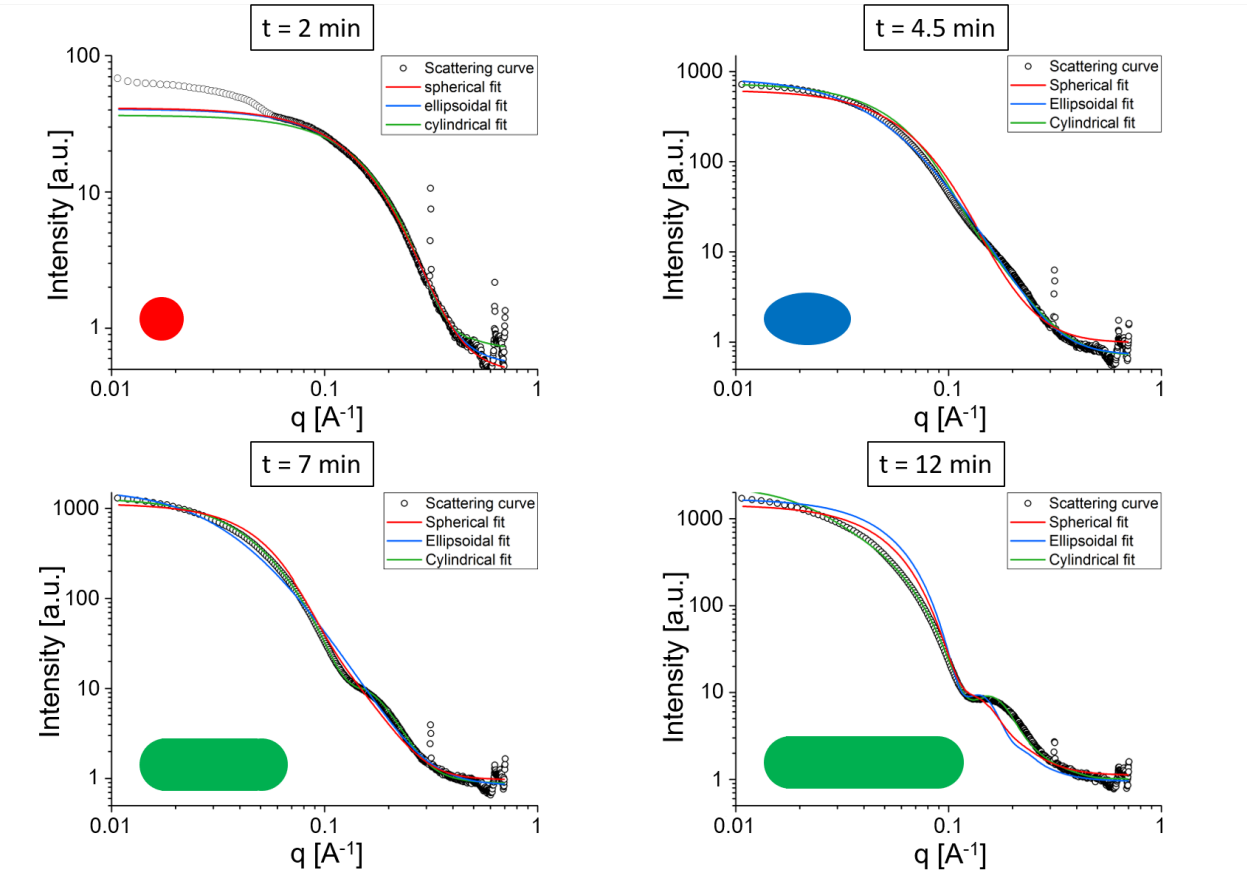

Figure 3: SAXS curves collected at different times during synthesis S3 and the associated fits obtained using spherical, ellipsoidal and (spherically capped) cylindrical models. The fits were obtained using eqs.7 and 9 (see Appendix). To account for the CTAB surfactant a shell layer is included as discussed in Section (VI).

Assuming a dilute system, the Guinier region at low q is related to the radius of gyration of the particles in solution.[29] For q greater than the Guinier region the shape of the scattering intensity demonstrates a strong q-dependence. For spherical particles in the scattering volume this dependence is between q^{-3} (rough or diffuse surfaces) to q^{-4} Porod-

decay (smooth, sharply defined surfaces). For cylinders the slope is a q^{-1} decay. These q dependencies are not unique to those shapes, but given the supporting information from microscopy, the variation in q dependence can be reliably utilised to track shape change *in situ*.

Figure 3 top left shows the SAXS data for sample S3 at the start of the synthesis, t = 2 minutes. The Guinier plateau in the regime where $q < 0.06\text{Å}^{-1}$ has a clear q^0 slope, leading to the Fourier region at $q > 0.06\text{Å}^{-1}$ with a Porod-decay between q^{-3} and q^{-4}. This indicates the presence of small spherical particles, i.e. the gold seed particles with radii $\sim$ 1.6 nm, which is confirmed by the best fit using equation 7 for core-shell spheres (red curve). During the course of the synthesis, the scattering intensity increases, corresponding to an increasing total volume of scattering particles in the solution. This is an indication of growing gold nanoparticles, since there is no new nucleation and the number of seed particles is fixed (or decreases). At later stages in the synthesis, we see the evolution of a pronounced form factor oscillation with a minimum shifting from around q = 0.2 Å^{-1} to approximately q = 0.1 Å^{-1} corresponding to the growth of monodisperse nanorods, as is also evident from the emergence and red-shift of the longitudinal plasmon peak in the UV-Vis spectra (see Figure 9). Furthermore, as the reaction time increases, the slope of the Guinier plateau increases, indicating a shape transition from spheres to cylindrical shape. From the fits, we obtain the scattered intensity $I(0)$, the mean radius R and mean length L of the particles, as well as the relative polydispersity in radius σ_R and length σ_L.

At the next timepoint in the synthesis at around 4.5 minutes, shown in Figure 3 top right, a steeper slope is evident. The fitting parameters for spherical particles, shown in red, do not fit the scattering curve well at this point. The Guinier plateau, which has shifted to lower q-range ($q < 0.03$ Å^{-1}), shows a decay between q^0 and q^{-1}, and the Fourier region ($q > 0.03$ Å^{-1}) exhibits the first signs of a form factor oscillation at higher q. These shoulders indicate a growth in size as well as a simultaneous change in shape. The best fit is achieved with a

core-shell ellipsoid model (blue curve) using equation 9.

III. Nanorod Growth

Figure 3 (bottom) displays scattering data collected at 7 and 12 minutes, from which it is evident that the Guinier region has now shifted to even lower q, and the Fourier region at intermediate q now evinces a clear q^{-1} slope, while the form factor oscillation has become more prominent. The best fit is achieved using a core-shell, spherically-capped cylinder model (equation 23), shown in green. We have also examined whether the measured scattering curves at this time can be described by spherical (red) or ellipsoidal (blue) particle models, but we find very poor agreement with the measured data, which supports the view that the nanoparticles at this stage have already adopted a cylindrical shape. We find that in all cases the contribution to the scattering from single growing nanorods dominates the measured scattering intensity, in particular in the Fourier region at $q > 0.06$ Å^{-1}, where we obtain information on the radius and polydispersity of the growing nanorods.

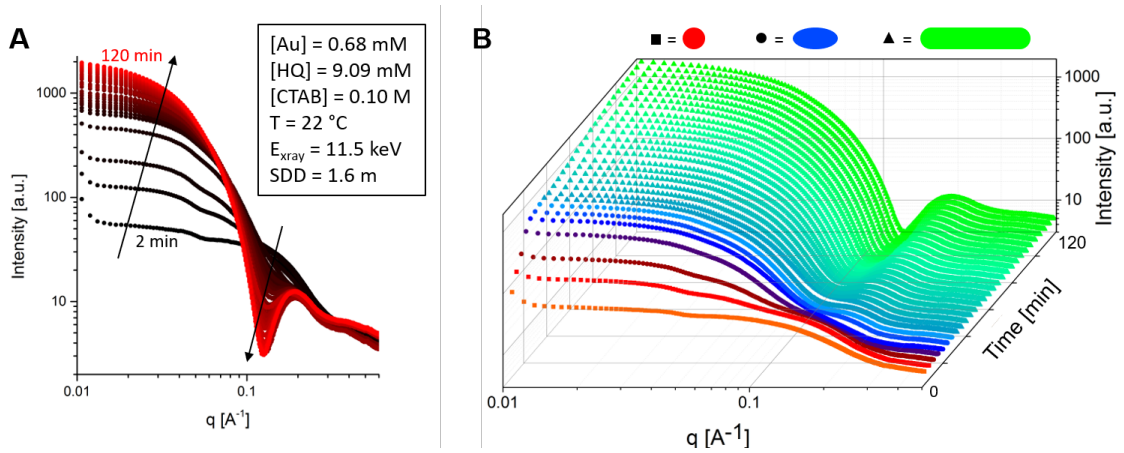

Figure 4: (A) Two-dimensional, time-resolved SAXS intensity as a function of scattering vector q for sample S4. The solid lines in the waterfall plot are fits using a cylindrical form factor. The scattering signal indicates a shift from spherical to rod-shaped particles and an increase in volume over time. (B) "Waterfall" plot showing the shape transition from sphere (orange to red) to ellipsoid (blue) to spherically capped cylinder (aqua or green) as a function of the reaction time. The reaction time was 2 hours with spectra collected every 2 minutes.

Figure 4 shows the scattered intensity I(0) as a function of the time for the synthesis conditions S4, providing systematic information on the gold nanorod growth. The SAXS intensity is plotted as a function of the scattering vector q in 2 min intervals over 120 min of reaction time. At the beginning of the synthesis, where only the initial spherical gold seeds are present in the growth solution, we observe a Guinier plateau at low scattering vectors q, which develops into a q^{-4}-Porod decay at $q > 0.1\text{Å}^{-1}$, followed by a shoulder at $q \sim 0.2$ Å^{-1} corresponding to the damped form factor oscillation of the spherical nanoparticles in dilute solution. The first five measurements (Fig. 4B red coloured curves) show a strong increase in scattering intensity, indicating the early volumetric growth of the seed particles. Subsequently, the form factor oscillation shifts to lower q, indicating an increase in the nanoparticle size during the growth phases. The observation of damped form factor oscillations indicates that narrowly disperse nanoparticles grow in solution.

Following the initial, fast growth step, there is a steady increase in scattering intensity but almost no shift in the Porod-shoulder (see Fig. 4B, blue coloured curves). This demon-

strates that the particles in solution grow mainly in volume rather than in radial size, which in turn implies a shape change. The curves at this time can be fitted by ellipsoidal particle models with increasing anisotropy factors.

The measurements after this point show a second rapid growth phase with a simultaneous increase in scattering intensity as well as the development of a more profound oscillation trough from the Porod-shoulder of the initial phases, shifting to lower q-range over time. We have assigned these scattering curves (Fig. 4B green) to spherically capped cylinders. The transition from sphere to ellipsoid to rod is determined by the lowest χ^2 value (with χ^2 close to 1 for a fit of the area of interest between 0.01 and 0.3 Å^{-1}). For all three shapes "core-shell" models have been used to take into account the contributions from the CTAB-ligand shell (see Section (v)). A detailed description of the mathematical models and the fitting criteria for each shape can be found in the Appendix. The SAXS data reveal that there is a well-defined transition from spherical seeds to ellipsoidal geometry and finally to a rod morphology during the reaction. The exact time at which this symmetry breaking occurs depends on the solution conditions but typically occurs around 5-6 minutes after growth of the seeds is initiated, which is consistent with numerous other reports.[20,30,31]

IV.Effect of [$HAuCl_4$] and [HQ]

In Figure 5, we show the key data gleaned from this study. For samples S1-S9, we show the time-resolved mean length and mean width of the rods as a function of time for different [$HAuCl_4$] and [HQ]. Note that for almost all of these data, the best fits were obtained using a spherocylindrical model, and so the trends are not artefacts due to the use of different morphologies for the fits. The results immediately highlight the complexity of gold nanorod formation and growth. There are different stages to the synthesis, which we delineate. These are:

Phase 1 - Initial growth and symmetry breaking between 0-6 minutes; Phase 2- A slow growth phase lasting just 5 - minutes for S3 but nearly 60 minutes for S7; during this time rod growth appears to be almost coming to completion; Phase 3- A secondary fast growth phase. The length undergoes rapid increases while the width may only increase minimally or weakly;this starts at t $\sim$ 10 minutes for S3 but at t $\sim$ 70 minutes for S7. We also believe that a less obvious fourth phase, where the width undergoes a secondary growth stage is discernible in experiments S1, S2 and S9 near the end of the reaction. The timepoints marking the onsets of the three key phases are indicated in Figure S12.

The SAXS data reveal that symmetry breaking occurs early and the subsequent rod growth exhibits syncopation or irregular growth rates. The length and width of the gold rod appear to grow independently with different factors determining the speed at different time points. In other words, at some points of the reaction both the rod length and width are increasing but at other timepoints, only the width or rod length is increasing significantly. Importantly, although there is an initial symmetry breaking event soon after measurement commences, the biggest change in aspect ratio occurs during the third phase of reaction,something which has not been reported previously.

Comparing S1-S3, where the [HQ] is increasing, we see that the final length decreases from 45 to 35 nm while the width is more or less the same at $\sim$ 8nm. There is faster rod growth during phase 1 at higher [HQ] and phase 2 is shorter and the start of phase 3 merges into phase 1. The width grows rapidly to around 6nm and then plateaus. Interestingly, for all reactions S1-S9, our data show that the particles have a diameter of around 6 nm when phase 3 occurs. This suggests that the tip facets enabling rod growth cannot form until the rod reaches a critical diameter. The critical diameter depends on the reductant used and solution parameters, as shown by Walsh et al.[7]

Comparing S4-S6 with S1-S3, we observe similar trends but we note that increasing [$HAuCl_4$] slows down the initial growth of the rods in phase 1, while the final rods are both longer and wider. Since the concentration of gold ions is the same in each reaction, this

means that fewer nuclei have survived. Increasing [$HAuCl_4$] delays the onset of phase 3, possibly because it takes the width longer to reach the critical width of 6nm. We also see that during phase 3, the width also undergoes accelerated growth.

These trends are clearly complex to interpret but it is not surprising that higher reductant concentrations speed up the rate of formation of gold rods, while Au(III) ions, which can effect gold metal oxidation seem to promote dissolution of nuclei and slower growth.

By comparing other sets of experiments e.g. S1 and S8, we can see that, if the gold ion concentration is increased at a fixed [$HAuCl_4$]: [HQ] ratio, the final aspect ratio does not change significantly. This reflects the opposing effects of the two reagents on the rod growth.

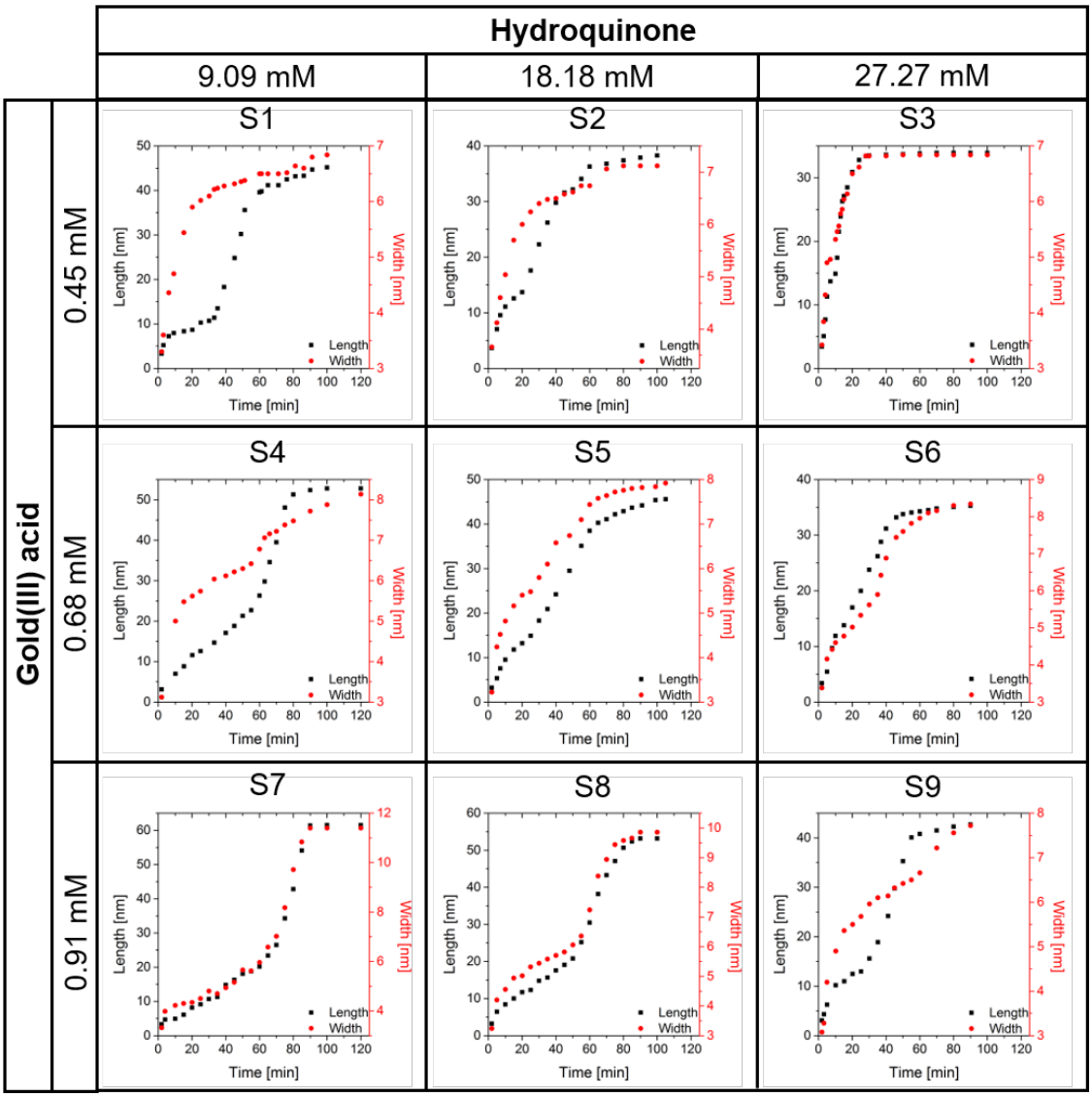

Figure 5: Time evolution of the length (black squares) and width (red circles) for samples S1-S9 determined from in-situ SAXS measurements.[CTAB] = 0.1 M, [$AgNO_3$] = 0.45 mM. Au seed concentration = $2.80 \cdot 10^{12}$ particles per mL. T=22^{o}C. [HQ] = 9.09 mM, 18.18 mM and 27.27 mM; [$HAuCl_4$] = 0.45 mM, 0.6 8mM and 0.91 mM.

In our SAXS experiments, the largest error is the determination of the mean particle size and morphology of the smallest seeds, so the exact timepoint at which symmetry breaking occurs is difficult to ascertain. The concentrations of both HQ and $HAuCl_4$ have a strong influence on the exact timepoint at which rod formation occurs. For example, consider reactions S1-S3 where the gold concentration is lowest and we have increasing reductant concentrations. We see that in S1, the length of the rods hardly increases from 8 nm at t =

5 minutes to 11 nm at t = 40 minutes, while the width doubles from around 3.5 nm to 6.5 nm. Between 40 and 60 minutes the rod undergoes drastic expansion, growing from 11 nm to 40 nm while the width hardly changes at all. Clearly, different facets of the rod undergo quite different rates of growth throughout the reaction. From 60 -100 minutes, both the length and width then undergo slower, 'incremental' growth.

The loss of gold seeds is however surprising in a solution containing a reducing agent but it is unambiguous. Comparing S1 to S2 and S3, we see that the final rod length decreases from 46 nm to 38 nm to 33 nm. The final width, irrespective of the dynamics, is around 7 nm in all cases. Hence, the final volume of the particles decreases, which implies that the number of gold rods increases with increasing [HQ]. The final number of rods is not the same as the number of seeds at the start of the reaction. Hence we conclude that not all seeds survive the reaction and some must undergo dissolution via Ostwald ripening. This is important since it implies that there is concurrent oxidation and reduction occurring continuously during the formation of gold rods. Although one might expect that increasing the reductant concentration would increase the rate of reduction and perhaps cede larger rods, we observe the opposite trend. Instead, this suggests that the reductant "protects" the gold seeds from oxidation, leading to a larger number of surviving seeds and ultimately this leads to a larger population of smaller aspect ratio rods.

Finally, we also note that the reaction is faster at higher [HQ], which is expected since this is the active reductant driving gold formation. Overall, the final rod length is reached in roughly 1/3 of the time for a tripling of the [HQ].

We now consider syntheses S1, S4 and S7. The most obvious trend here is that the final rod length increases with increasing [$HAuCl_4$]. There is also a substantial increase in the final gold rod width from 6.8 nm up to 11.5 nm. Again this implies that there are fewer

rods overall with increasing [$HAuCl_4$]. The transition from phase 2 to phase 3 is less sharp as [$HAuCl_4$] increases and phase 3 occurs at longer times. The strong growth in the rod width seen in phase 2 for S1 is significantly weaker and from 0 - 60 minutes, the width only increases from 4 nm to 6 nm.

Phase 3 is actually when most of the gold nanoparticle elongation occurs. Extrapolating the linear part of phase 3 back to the x-axis,shows that this phase starts at the 25 minute mark for S1, the 45 minute mark for S4 and at the 60 minute mark for S7. Rod growth occurs sooner for lower [$HAuCl_4$] and furthermore it occurs when the rods are longer for higher [$HAuCl_4$]. Hence gold chloride slows down the start of the rod growth spurt. This later time also means the rod has grown longer before it starts and hence this leads to longer rods at the end of reaction.

We clearly see that while there is always rod growth through phases 1, 2 and 3, the relative rates of growth of the width and length change drastically. Comparing S7, S8 and S9 we see again that the final rod width decreases slightly while the final rod length decreases very significantly from 60nm to around 40nm. In Figure S8, we plot these curves to highlight the effects of changing concentration more clearly.

V. Model-Free SAXS Analysis

Modern SAXS analysis uses computational methods combined with user-inputted models of the particle morphology. It might be argued that the observed trends are a result of the fitting process. However, as the intensities of the SAXS patterns are scaled to absolute intensities, we can also evaluate the SAXS data using a model-free method.[29] By fitting and extrapolating Guinier plots (shown in Figure 6), we obtain the zero angle intensity I(0) as a function of time from the intercept of each fit. Furthermore, from the slope of the fit functions, we can calculate the radius of gyration, shown as a function of time for S3 in Figure 6 (black squares) according to the well-known Guinier approximation:

$$I(q) = I(0)exp\left(-\frac{q^2R_g^2}{3}\right) \tag{2}$$

Figure 6 shows the model-free Guinier analysis for synthesis S3. The time dependent plots of I(0) and radius of gyration for gold nanorods S1, S3, S4 and S6 can be found in the Supplementary Information (Figures S3 and S4). The intensity can be used to estimate the volume of the particles while the slope gives the radius of gyration.

While we obtain very good fits for the Guinier region in the early stages of the reaction (see Figure 6 B), the fits become less accurate over time as the number of data points available decreases. This is simply due to the fact that as the nanocrystals increase in volume and size, the Guinier region of the SAXS pattern is shifted to lower q-values, which results in less accurate fitting. Nevertheless, we do observe an increase in I(0) and R_g, which parallels the observed increases in the rod length and width deduced from the model-dependent fitting of the data, (see Figure 6 C and D, respectively). As the radius of gyration is directly dependent on the size of the observed particles, an increase in R_g indicates an increase in the size of the crystals. Similarly, I(0) depends on the square of the particle volume, allowing the relative changes in volume to be followed quite accurately. This model-free analysis of the growth process is consistent with the model-dependent fitting discussed earlier.

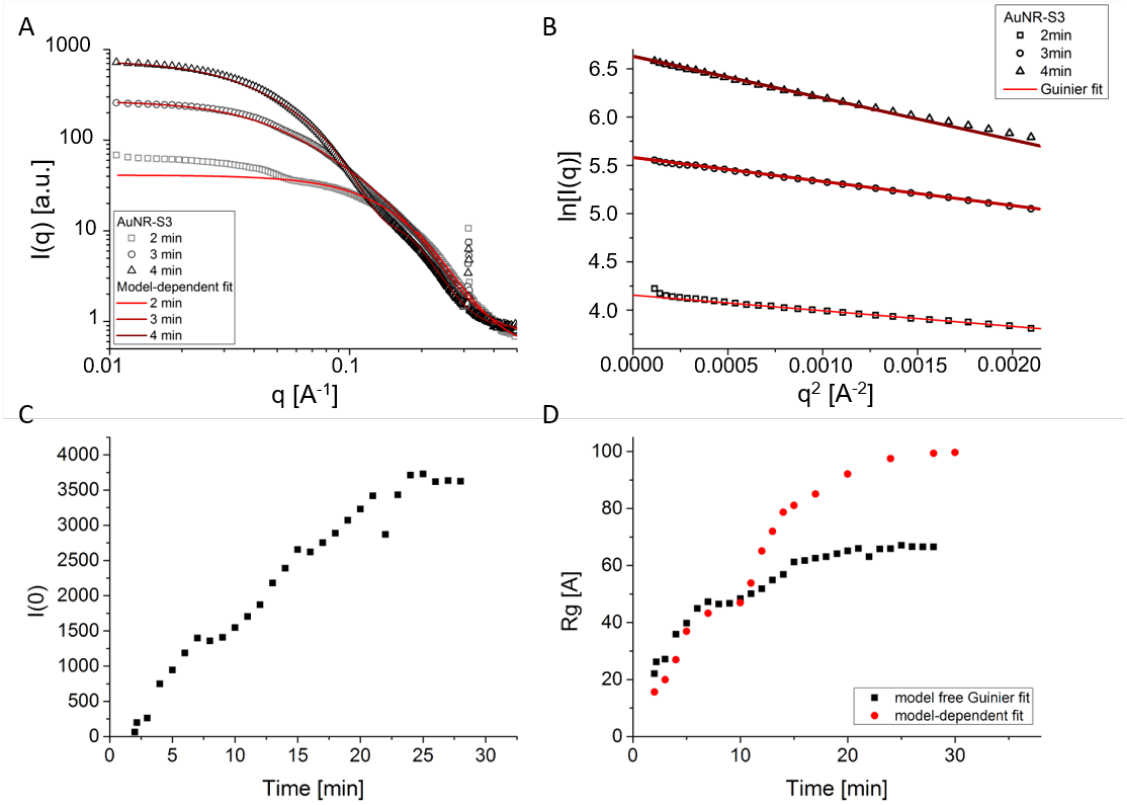

Figure 6: Guinier analysis of the synthesis S3. (A) Log-log representation of the first 3 measurements at 2, 3 and 4 minutes after seed addition of synthesis S3 with respective model-dependent fit (red). (B) Guinier plot of (ln(Intensity) versus the square of the scattering vector q) for the first 3 measurements of S3 associated fit (red). (C) Extrapolated zero angle intensity I(0) as a function of time. (D) Radius of gyration obtained from the slope of Guinier fits as a function of time (black squares) in comparison to the calculated radius of gyration from resulting values from length and radius from model dependent fits (red circles).

The theoretical radius of gyration, R_g, can be calculated from known length, L, and width, R, of the gold particles at any point during the synthesis using the following approximation for cylinders:

$$R_g^2 = \frac{L^2}{12} + \frac{R^2}{2} \tag{3}$$

One has to be cautious in making direct comparisons of the data, as there are several assumptions made for the determination of R_g from Guinier plots. Firstly, it is assumed that the structure factor can be ignored, which is true for dilute solutions. However, in

the final stages of the reaction, it is possible that the concentration of particles in solution and their size might influence the structure factor. Secondly, background-subtracted data is necessary for Guinier plot extrapolation. We have used 0.1 M CTAB solution as the background reference; however, the background subtraction becomes difficult in the late stages of the synthesis, as the concentration of free CTAB micelles in solution decreases in favour of CTAB-shell-formation on the growing gold nanorods. Thirdly, the reduced amount of data available for fitting in the late reaction stages leads to higher errors in the resulting R_g values. We also find that in the early stages of the reaction, the particles are more polydisperse in length and shape than in the later stages. This polydispersity is evident in the first scattering patterns obtained (Figure 6 A) and makes Guinier extrapolations for I(0) and R_g difficult.

VI. CTAB Layer

While the fits to spheres and cylinders are adequate, a better fit for almost all the curves can be obtained when a core-shell model is adopted to evaluate the SAXS data (see Appendix for equations). The shell layer accounts for the X-ray scattering from the CTAB layer around the rods. This introduces a second parameter, the CTAB layer thickness, into the modelling.

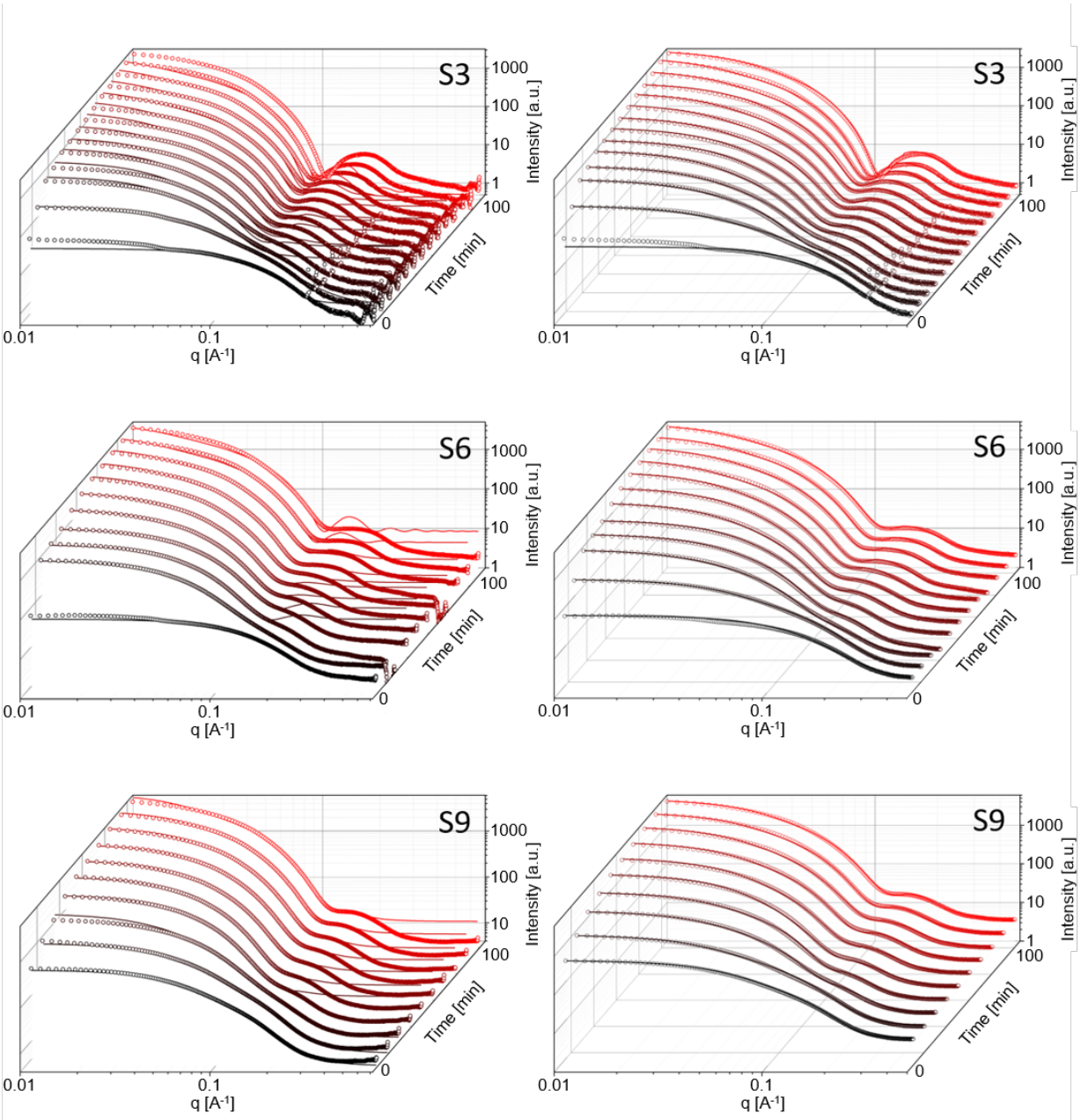

Figure 7: Waterfall plots of the SAXS data including the fits for spherical, ellipsoidal and cylindrical particles as a function of time for three different syntheses (S3, S6 and S9). Left: Fit without a shell. Right: Fit using a core-shell model.

Figure 7 presents the SAXS curves obtained during the experiments for syntheses S3 (top), S6 (centre) and S9 (bottom) along with the corresponding fits without (left) and with a shell (right). For all the experiments, inclusion of the shell gives better fits to the data.

We consistently find that the CTAB layer thickness is 3.1 nm $\pm$ 0.3 nm, corresponding

to a bilayer around the gold rods.[32] The CTAB thickness is shown in Figure 8 (right) as a function of reaction time for synthesis S1. Inclusion of the CTAB layer modifies slightly the values of the length and width gleaned from the SAXS data.

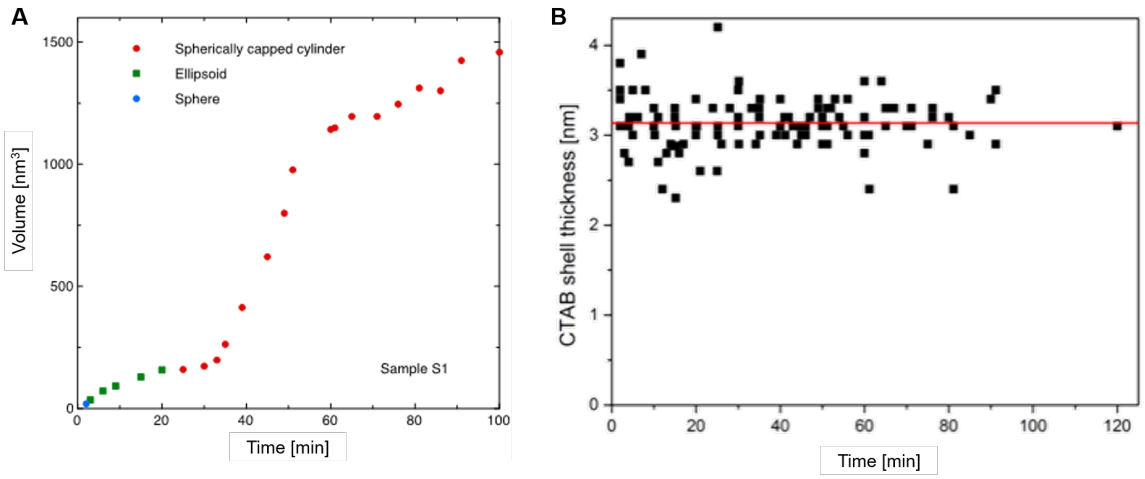

Figure 8: (A) Calculated volume vs time for sample S1. Length and width fitted to 3 different shapes as the reaction progresses. There is an initial induction at time 0 - 3 minutes. The reaction appears to finish at 30 minutes but then accelerates rapidly up to the 60 min. mark. Further weak growth then occurs up to the 80 minute mark. (B) CTAB layer thickness from SAXS core-shell fit for different shapes for all investigated syntheses over time, and a linear fit giving an average thickness of 3.1 nm $\pm$ 0.3 nm.

VII. UV-vis Spectroscopy

It is important to confirm that the gold rods grown in the capillaries used in the SAXS measurements are the same as those grown in conventional batch reactors. In Figure S2, we show the position of the LSPR band as a function of time for two identical preparations (nominal conditions same as S7). We find that the spectral shifts are the same within experimental error. This shows that the capillary walls do not influence the nucleation and growth of the rods on the timescale of the experiments. Hence the data presented here should be applicable to conventional lab reactions.

In Figure 9 we have plotted the observed LSPR peak wavelength as a function of reaction time for all reactions S1-S9. These have been collected at the same time as the SAXS data. The actual peakk wavelengths are all collected in Table S1. In qualitative agreement with the SAXS data, we see that in any series of 3 experiments where $[HAuCl_4]$ is fixed, an increase in the [HQ] leads to a final peak position at shorter wavelengths (compare S1 and S2 and S3), whereas increasing $[HAuCl_4]$ at fixed values of [HQ] leads to a final peak at longer wavelengths. Typically we also see that reactions terminating at lower wavelengths are faster and the LSPR shifts are faster vs time.

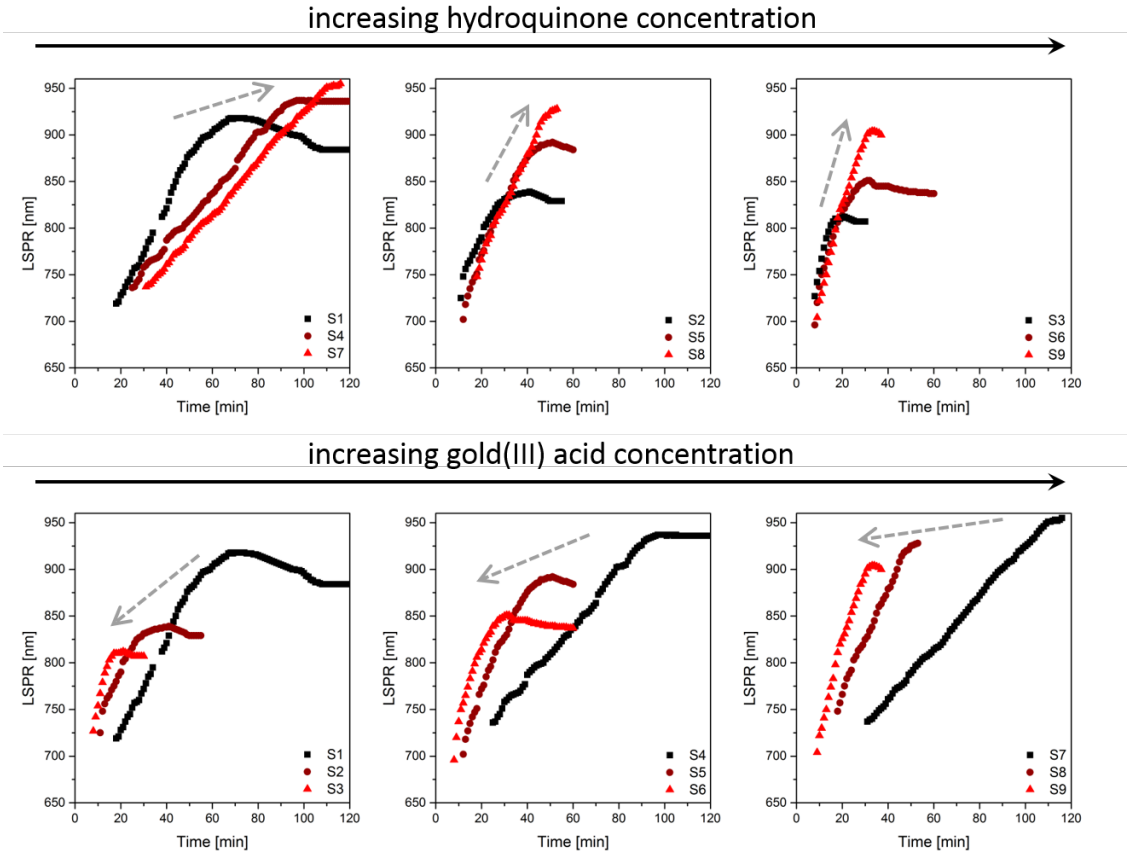

Figure 9: The position of the longitudinal surface plasmon resonance peak wavelength as a function of time for reactions S1-S9. Reactions carried out in capillary during in-situ SAXS measurements and recorded via optic fibre. (top): Reactions showing the effect of increasing [HQ] on the peak position (left to right) for increasing gold concentrations (gray arrows); (bottom): Reactions showing effect of increasing $[HAuCl_4]$ on peak position for increasing hydroquinone concentrations (gray arrows).

In contrast to the SAXS data, the LSPR peak often exhibits a blue-shift near the end of the reaction. It is unclear from the UV-vis spectra alone whether this is due to changes in endcap geometry or decreases in the aspect ratio. However the SAXS results demonstrate that the rods do not decrease in aspect ratio even at longer times, so these shifts reflect a further change in crystal morphology, i.e. endcap geometry. Despite the excellent size resolution of the SAXS measurements, we still had some difficulty to accurately fit the experimental UV-vis spectra at the end of the reaction using the SAXS data.The SAXS spectra can be fitted using either an intensity weighting or number weighting (see Table S6). Inputting these data into a COMSOL models yields two predicted spectra for the surface plasmon resonance of each sample and these are shown together with the experimental spectra in Figures S13-15. While the agreement is not as good as expected, inclusion of polydispersity would improve the fits.

CONCLUSIONS

The growth of gold nanorods provides an important model for understanding the factors that determine crystal morphology. Until now nanocrystal growth has often been modelled using conventional chemical kinetic models and these have been very successful in some cases such as Ir nanocrystal[33,34] and CdSe nanocrystal growth.[35] However, our data show that anisotropic growth dynamics are far more complex. Following early symmetry breaking, the length and width of the rods increase in a complex manner with the actual growth velocities (atoms per m^2 per second) increasing and decreasing throughout the reaction. However, there is a steady increase in aspect ratio. Most spectacularly, there is a characteristic, "explosive" growth phase observed at the 40-60 minute mark, depending on reaction conditions, which is far more important for determining the final rod aspect ratio. The nature of this secondary growth phase exhibits a clear dependence on the HQ and $HAuCl_4$ concentrations. Surprisingly, the concentration of silver ions does not play a role in determining the onset of

this growth phase, indicating that the primary role of silver is to initiate symmetry breaking. The time resolved synchrotron SAXS data reveal that the growth of gold nanorods is a rich and complex process but the following clear trends are revealed when both width and length can be quantified as a function of reaction time:

(i) The rate of gold rod growth increases with increasing hydroquinone concentrations, but decreases with increasing [$HAuCl_4$] concentration;

(ii) The final length increases with increasing [$HAuCl_4$]-concentration;

(iii) The final length decreases with increasing hydroquinone concentration;

(iv) Initial symmetry breaking occurs in the first $\sim$ 6 minutes (which we call phase 1) but the rate of growth often slows down after this, although some increase in aspect ratio is observed (phase 2). The relative rates of lateral and longitudinal growth depend on the concentration of reactants. Phase 2 can be relatively short (5 minutes) or long (50 minutes), depending on the gold ion and HQ concentrations.

(v) At the end of phase 2, there is a second growth stage, which marks the onset of strong rod growth (phase 3). The time at which this stage occurs depends on the initial concentrations of [$HAuCl_4$] and hydroquinone, but is independent of the [$AgNO_3$]. Under conditions where there is high [$HAuCl_4$], this critical growth regime begins around 60 minutes after the reaction starts. It is probably masked during synthesis using ascorbate reduction by the faster rate of reaction.

(vi) Based on the UV-vis spectra, there is a further, weaker, growth stage which appears occurs around 80 minutes, which marks the break from pure, spherically-capped-cylinder

geometry. This is marked by a blue-shift in the absorption spectrum and is weakly evident in several of the SAXS curves. It may coincide with changes in rod width, which are evident at late stages in reactions S1, S2 and S9.

(vii) The final concentration of rods is not the same as at the starting seed concentration. Since uniform nanorods are formed, the number of surviving nuclei is inversely proportional to final particle volume. Ostwald ripening increases with increasing [$HAuCl_4$] and decreases with increasing [HQ]. We can compare the largest rods (S7) to the smallest (S3) and note that the former have about 5 times the volume of the latter, despite starting with identical concentrations of seeds and only twice as much gold salt (0.91mM vs 0.45mM). This implies that about 60% of the seeds are annihilated in S3.

There have been numerous electron microscopy studies of the evolution of gold rods as they grow. These studies have highlighted the importance of both symmetry breaking[7,30] and the fact that the shape continues to evolve throughout the reaction.[36] The data here suggest that the width and length are growing independently but that changes in the solution composition dictate which facets grow most strongly at different stages of the reaction.

Sample S1 is perhaps the most striking gold rod synthesis. It clearly shows that symmetry breaking does not unlock rod growth. Symmetry breaking itself occurs early but this is followed by an asymptotic decline in the rate of rod growth. At a critical time it begins again. In some cases this decline in rate is less obvious because phase 3 occurs earlier if the [HQ] is high enough and [$HAuCl_4$] low enough. Under the opposite conditions, phase 3 occurs very late and it is observable in both SAXS data and in UV-vis spectroscopy. For example in SI Figure S10 there is a clear jump in the LSPR peak during the reaction. We can see this peak in the work of previous researchers but it has not been commented on in those papers.[36,37]

Our TEM and SAXS data do not reveal any evidence for significant secondary populations of spheres or smaller rods, as would be expected if rod dissolution occurred continuously. Indeed if Ostwald ripening occurred throughout the reaction, one would not obtain such monodisperse rod solutions at the end of the experiment. This suggests that seed dissolution occurs primarily in the early phases. This must occur due to conproportionation of the gold salts with the metal gold seeds:

$$2Au^0 + AuBr_4- \longrightarrow 3AuBr_2- \tag{4}$$

Au(III) dissolves gold atoms in competition with their deposition by Au(I). This has been shown by watching the etching of gold rods when $HAuCl_4$ is added.[38] Why this occurs is complex but given how slow rod growth is, it is possible that the disproportionation reaction

$$3AuBr_2- \longrightarrow 2Au^0 + AuBr_4- \tag{5}$$

controls rod growth. It has been postulated that the rate of gold metal growth is rate limited by the availability of kink sites.[39,40] If this is true, then since kink sites are most common on high index facets,[6,41,42] the fast growth phase (phase III) may be explained most easily by the emergence of high index facets which in turn leads to increasing numbers of kink sites on the surface. The unusual growth rate observed here supports the "popcorn" model proposed by Edgar et al.[24]

APPENDIX

The following equations were used to fit the scattering data. The curves were often fitted by two different forms and the better one was then used to determine the particle shape and size.

Sphere

The 1D scattering intensity is calculated in the following way

$$P(q) = \frac{scale}{V} \cdot \left[3V(\Delta\rho) \cdot \frac{\sin(qr) - qr\cos(qr)}{(qr)^3} \right]^2 + background \tag{6}$$

where *scale* is a volume fraction, V is the volume of the scatterer, r is the radius of the sphere and *background* is the background level. $\Delta\rho$ is the difference between scattering length density of the scatterer and the solvent.[29]

Core-shell sphere

The 1D scattering intensity is calculated in the following way

$$P(q) = \frac{scale}{V} F^2(q) + background \tag{7}$$

where

$$F^2(q) = \frac{3}{V_s} \left[V_c(\rho_c - \rho_s) \frac{\sin(qr_c) - qr_c\cos(qr_c)}{(qr_c)^3} + V_s(\rho_s - \rho_{solv}) \frac{\sin(qr_s) - qr_s\cos(qr_s)}{(qr_s)^3} \right] \tag{8}$$

where V_s is the volume of the whole particle, V_c is the volume of the core, $r_s = radius + thickness$ is the radius of the particle, r_c is the radius of the core, ρ_s is the scattering length density of the shell and ρ_{solv} is the scattering length density of the solvent.[29]

Ellipsoid

The output of the intensity function for ellipsoids is given by

$$P(q) = \frac{scale}{V} F^2(q) + background \tag{9}$$

where

$$F(q) = \frac{3\Delta\rho V(\sin[qr(R_p, R_e)] - \cos[qr(R_p, R_e)])}{[qr(R_p, R_e)]} \tag{10}$$

and

$$r(R_p, R_e) = \left[R_e^2 + R_p^2\right]^{\frac{1}{2}} \tag{11}$$

$V = (\frac{4}{3})\pi R_p R_e^2$ is the volume of the ellipsoid, R_p is the polar radius along the rotational axis of the ellipsoid, R_e is the equatorial radius perpendicular to the rotational axis of the ellipsoid and $\Delta\rho$ (contrast) is the scattering length density difference between the scatterer and the solvent.[43]

Core-shell ellipsoid

The geometric parameters of this model are the core axial ratio X and the shell thickness T given by

$$r_{equat_{core}} = equatorial\ core\ radius = R_{minor_{core}} \tag{12}$$

$$X_{core} = \frac{polar_{core}}{r_{equat_{core}}} = \frac{R_{major_{core}}}{R_{minor_{core}}} \tag{13}$$

$$T_{shell} = r_{equat_{outer}} - r_{equat_{core}} = \frac{R_{major_{core}}}{R_{minor_{core}}} \tag{14}$$

$$X_{polar_{shell}} = \frac{T_{polar_{shell}}}{T_{shell}} = \frac{(R_{major_{outer}} - R_{major_{core}})}{(R_{minor_{outer}} - R_{minor_{core}})} \tag{15}$$

In terms of original radii

$$polar_{core} = r_{equat_core} \cdot X_{core} \tag{16}$$

$$equat_{shell} = r_{equat_{core}} + T_{shell} \tag{17}$$

$$polar_{shell} = r_{eqaut_{core}} \cdot X_{core} + T_{shell} \cdot T_{polar_{shell}} \tag{18}$$

where shell relates to the outer radius. When $X_{core} < 1$ the core is oblate, when $X_{core} > 1$ it is prolate. $X_{core} = 1$ is a spherical core.[44,45]

Spherically capped cylinder

Capped cylinder geometry, where r is the radius, R is the bell radius and L is the length.[46] For the curve fit, the bell radius was set equal to the cylinder radius. When the end cap radius $R \geq r$, then by definition for this geometry $h < 0$, with h being defined by r and R as $h = -\sqrt{R^2 - r^2}$.

The scattered intensity $I(q)$ is calculated as

$$I(q) = \frac{\Delta\rho^2}{V}\langle A^2(q)\rangle \tag{19}$$

where the amplitude $A(q)$ is given as

$$A(q) = \pi r^2 L \frac{\sin\left(\frac{1}{2}qL\cos\theta\right)}{\frac{1}{2}qL\cos\theta}\frac{2J_1(qr\sin\theta)}{qr\sin\theta} + 4\pi R^3 \int_{-\frac{h}{R}}^{1} \cos\left[q\cos\theta\left(Rt + h + \frac{1}{2}L\right)\right]dt\cdot \tag{20}$$

$$\cdot(1-t^2)\frac{J_1\left[qR\sin\theta(1-t^2)^{\frac{1}{2}}\right]}{qR\sin\theta(1-t^2)^{\frac{1}{2}}}$$

The $\langle ... \rangle$ brackets denote an average of the structure overall orientations. $\langle A^2(q)\rangle$ is then

the form factor, $P(q)$. The scale factor is equivalent to the volume fraction of cylinders, each of volume V. Contrast $\Delta\rho$ is the difference of scattering length densities of the cylinder and the surrounding solvent.[47] The volume of the capped cylinder is (with h as a positive value)

$$V = \pi r_c^2 L + \frac{2\pi}{3}(R-h)^2(2R+h) \tag{21}$$

and its radius of gyration is

$$R_g^2 = [\frac{12}{5}R^5 + R^4\left(6h + \frac{3}{2}L\right) + R^2(4h^2 + L^2 + 4hL) + R^2\left(3Lh^2 + \frac{3}{2}L^2h\right) + \frac{2}{5}h^5 \tag{22}$$

$$-\frac{1}{2}Lh^4 - \frac{1}{2}L^2h^3 + \frac{1}{4}L^3r^2 + \frac{3}{2}Lr^4]\ (4R^36R^2h - 2h^3 + 3r^2L)^{-1}$$

Core-shell cylinder

The output of the intensity function for oriented core-shell cylinders is given by

$$I(q) = \frac{scale}{V_s}F^2(q) + background \tag{23}$$

where

$$F(q) = (\rho_c - \rho_s)V_c\frac{\sin\left(q\frac{1}{2}L\right)}{q\frac{1}{2}L}\frac{2J_1qR}{qR} + (\rho_s - \rho_{solv})V_s\frac{\sin\left(q\left(\frac{1}{2}L+T\right)\right)}{q\left(\frac{1}{2}L+T\right)} \tag{24}$$

and

$$Vs = \pi(R+T)^2(L+2T) \tag{25}$$

V_s is the volume of the outer shell (i.e. the total volume, including the shell), V_c is the volume of the core, L is the length of the core, R is the radius of the core, T is the thickness

of the shell, ρ_c is the scattering length density of the core, ρ_s is the scattering length density of the solvent and *background* is the background scattering level. The outer radius of the shell is given by $R + T$ and the total length of the outer shell is given by $L + 2T$. J_1 is the first order Bessel function.[48,49]

Calculation of Gold Rod Volume

(a) if sphere:

$$V = \frac{4\pi}{3}\left(\frac{width}{2}\right)^3 \tag{26}$$

(b) if ellipsoidal:

$$V = \frac{4\pi}{3}\left(\frac{width}{2}\right)^2\left(\frac{length}{2}\right) \tag{27}$$

(c) if spherically-capped cylinder:

$$V = \pi\left(\frac{width}{2}\right)^2(length - width) + \frac{4\pi}{3}\left(\frac{width}{2}\right)^3 \tag{28}$$

where width and length are determined from TEM measurements.

Supporting Information.

The Supporting Information is available free of charge on the ACS Publications website at DOI: ...

This contains extended results of the spectra from Figure 5, further SAXS data, discussions of the SAXS fitting procedure, tables of length and width and LSPR wavelengths for all reactions and details of the COMSOL modelling.

Author Information

Corresponding Author

* Paul Mulvaney, Phone +61 3 83442405, Fax +61 3 93481595, email: mulvaney@unimelb.edu.au

Author Contributions

The manuscript was written through contributions of all authors. All authors have given approval to the final version of the manuscript.

Acknowledgements

This work was financial supported by an ERC Advanced Grant (STREAM, #291211), by the German Ministry BMBF (#05K13WC5) and the German Science Foundation (DFG/GRK 1640). The authors acknowledge financial support by the German Academic Exchange Service (DAAD) through its Thematic Network, the Melbourne-Bayreuth Polymer/Colloid Network, sponsored from funds of the Federal Ministry of Education and Research (BMBF). S.S., H.Z. and P.M. acknowledge support through the ARC Centre of Excellence in Exciton Science (CE170100026). The authors also thank the staff of the Australian Synchrotron, ANSTO, where the SAXS experiments were performed at the SAXS / WAXS beamline through Grant number M11824.

References

(1) Yu,; Chang, S.-S.; Lee, C.-L.; Wang, C. R. C. Gold Nanorods: Electrochemical Synthesis and Optical Properties. *The Journal of Physical Chemistry B* **1997**, *101*, 6661–6664.

(2) Nikoobakht, B.; El-Sayed, M. A. Preparation and Growth Mechanism of Gold Nanorods (NRs) Using Seed-Mediated Growth Method. *Chemistry of Materials* **2003**, *15*, 1957–1962.

(3) Sau, T. K.; Murphy, C. J. Seeded High Yield Synthesis of Short Au Nanorods in Aqueous Solution. *Langmuir* **2004**, *20*, 6414–6420.

(4) Prescott, S. W.; Mulvaney, P. Gold nanorod extinction spectra. *Journal of Applied Physics* **2006**, *99*, 123504.

(5) Henkel, A.; Schubert, O.; Plech, A.; Sönnichsen, C. Growth Kinetic of a Rod-Shaped Metal Nanocrystal. *The Journal of Physical Chemistry C* **2009**, *113*, 10390–10394.

(6) Tong, W.; Walsh, M. J.; Mulvaney, P.; Etheridge, J.; Funston, A. M. Control of Symmetry Breaking Size and Aspect Ratio in Gold Nanorods: Underlying Role of Silver Nitrate. *The Journal of Physical Chemistry C* **2017**, *121*, 3549–3559.

(7) Walsh, M. J.; Tong, W.; Katz-Boon, H.; Mulvaney, P.; Etheridge, J.; Funston, A. M. A Mechanism for Symmetry Breaking and Shape Control in Single-Crystal Gold Nanorods. *Accounts of Chemical Research* **2017**, *50*, 2925–2935.

(8) Burrows, N. D.; Harvey, S.; Idesis, F. A.; Murphy, C. J. Understanding the Seed-Mediated Growth of Gold Nanorods through a Fractional Factorial Design of Experiments. *Langmuir* **2017**, *33*, 1891–1907.

(9) Katz-Boon, H.; Rossouw, C. J.; Weyland, M.; Funston, A. M.; Mulvaney, P.; Etheridge, J. Three-Dimensional Morphology and Crystallography of Gold Nanorods. *Nano Letters* **2011**, *11*, 273–278.

(10) Carbó-Argibay, E.; Rodríguez-González, B.; Gómez-Graña, S.; Guerrero-Martínez, A.; Pastoriza-Santos, I.; Pérez-Juste, J.; Liz-Marzán, L. M. The Crystalline Structure of Gold Nanorods Revisited: Evidence for Higher-Index Lateral Facets. *Angewandte Chemie* **2010**, *122*, 9587–9590.

(11) Niidome, Y.; Nakamura, Y.; Honda, K.; Akiyama, Y.; Nishioka, K.; Kawasaki, H.; Nakashima, N. Characterization of silver ions adsorbed on gold nanorods: surface analysis by using surface-assisted laser desorption/ionization time-of-flight mass spectrometry. *Chemical Communications* **2009**, 1754–1756.

(12) Langille, M. R.; Personick, M. L.; Zhang, J.; Mirkin, C. A. Defining Rules for the Shape Evolution of Gold Nanoparticles. *Journal of the American Chemical Society* **2012**, *134*, 14542–14554.

(13) Polte, J.; Erler, R.; Thünemann, A. F.; Sokolov, S.; Ahner, T. T.; Rademann, K.; Emmerling, F.; Kraehnert, R. Nucleation and Growth of Gold Nanoparticles Studied via in situ Small Angle X-ray Scattering at Millisecond Time Resolution. *ACS Nano* **2010**, *4*, 1076–1082.

(14) Polte, J. Fundamental growth principles of colloidal metal nanoparticles – a new perspective. *CrystEngComm* **2015**, *17*, 6809–6830.

(15) Hubert, F.; Testard, F.; Thill, A.; Kong, Q.; Tache, O.; Spalla, O. Growth and Overgrowth of Concentrated Gold Nanorods: Time Resolved SAXS and XANES. *Crystal Growth & Design* **2012**, *12*, 1548–1555.

(16) Hatakeyama, Y.; Sasaki, K.; Judai, K.; Nishikawa, K.; Hino, K. Growth Behavior of Gold Nanorods Synthesized by the Seed-Mediated Method: Tracking of Reaction Progress by Time-Resolved X-ray Absorption Near-Edge Structure, Small-Angle X-ray Scattering, and Ultraviolet–Visible Spectroscopy. *The Journal of Physical Chemistry C* **2018**, *122*, 7982–7991.

(17) Plech, A.; Kotaidis, V.; Siems, A.; Sztucki, M. Kinetics of the X-ray induced gold nanoparticle synthesis. *Physical Chemistry Chemical Physics* **2008**, *10*, 3888.

(18) Chen, X.; Schröder, J.; Hauschild, S.; Rosenfeldt, S.; Dulle, M.; Förster, S. Simultaneous SAXS/WAXS/UV–Vis Study of the Nucleation and Growth of Nanoparticles: A Test of Classical Nucleation Theory. *Langmuir* **2015**, *31*, 11678–11691.

(19) Ingham, B. X-ray scattering characterisation of nanoparticles. *Crystallography Reviews* **2015**, *21*, 229–303.

(20) Vigderman, L.; Zubarev, E. R. High-Yield Synthesis of Gold Nanorods with Longitudinal SPR Peak Greater than 1200 nm Using Hydroquinone as a Reducing Agent. *Chemistry of Materials* **2013**, *25*, 1450–1457.

(21) Tebbe, M.; Kuttner, C.; Mayer, M.; Maennel, M.; Pazos-Perez, N.; König, T. A.; Fery, A. Silver-Overgrowth-Induced Changes in Intrinsic Optical Properties of Gold Nanorods: From Noninvasive Monitoring of Growth Kinetics to Tailoring Internal Mirror Charges. *The Journal of Physical Chemistry C* **2015**, *119*, 9513–9523.

(22) Li, J.; Wang, W.; Zhang, X.; Yao, H.; Wei, Z.; Li, X.; Mu, X.; Jiang, J.; Zhang, H. Seedless preparation of Au nanorods by hydroquinone assistant and red blood cell membrane camouflage. *RSC Advances* **2018**, *8*, 21316–21325.

(23) Bullen, C.; Zijlstra, P.; Bakker, E.; Gu, M.; Raston, C. Chemical Kinetics of Gold Nanorod Growth in Aqueous CTAB Solutions. *Crystal Growth & Design* **2011**, *11*, 3375–3380.

(24) Edgar, J. A.; McDonagh, A. M.; Cortie, M. B. Formation of Gold Nanorods by a Stochastic "Popcorn" Mechanism. *ACS Nano* **2012**, *6*, 1116–1125.

(25) Johnson, P. B.; Christy, R. W. Optical Constants of the Noble Metals. *Physical Review B* **1972**, *6*, 4370–4379.

(26) Kirby, N. M.; Mudie, S. T.; Hawley, A. M.; Cookson, D. J.; Mertens, H. D. T.; Cowieson, N.; Samardzic-Boban, V. A low-background-intensity focusing small-angle X-ray scattering undulator beamline. *Journal of Applied Crystallography* **2013**, *46*, 1670–1680.

(27) Link, S.; Mohamed, M. B.; El-Sayed, M. A. Simulation of the Optical Absorption Spectra of Gold Nanorods as a Function of Their Aspect Ratio and the Effect of the Medium Dielectric Constant. *The Journal of Physical Chemistry B* **1999**, *103*, 3073–3077.

(28) Pecharromán, C.; Pérez-Juste, J.; Mata-Osoro, G.; Liz-Marzán, L. M.; Mulvaney, P. Redshift of surface plasmon modes of small gold rods due to their atomic roughness and end-cap geometry. *Physical Review B* **2008**, *77*, 035418.

(29) Guinier, A.; Fournet, G. *Small-Angle Scattering of X-rays*; Structure of matter series; New York, Wiley, 1955; Vol. 7.

(30) Walsh, M. J.; Barrow, S. J.; Tong, W.; Funston, A. M.; Etheridge, J. Symmetry Breaking and Silver in Gold Nanorod Growth. *ACS Nano* **2015**, *9*, 715–724.

(31) Vigderman, L.; Khanal, B. P.; Zubarev, E. R. Functional Gold Nanorods: Synthesis, Self-Assembly, and Sensing Applications. *Advanced Materials* **2012**, *24*, 4811–4841.

(32) Gómez-Graña, S.; Hubert, F.; Testard, F.; Guerrero-Martínez, A.; Grillo, I.; Liz-Marzán, L. M.; Spalla, O. Surfactant (Bi)Layers on Gold Nanorods. *Langmuir* **2012**, *28*, 1453–1459.

(33) Watzky, M. A.; Finke, R. G. Transition Metal Nanocluster Formation Kinetic and Mechanistic Studies. A New Mechanism When Hydrogen Is the Reductant: Slow, Continuous Nucleation and Fast Autocatalytic Surface Growth. *Journal of the American Chemical Society* **1997**, *119*, 10382–10400.

(34) Watzky, M. A.; Finke, R. G. Gold Nanoparticle Formation Kinetics and Mechanism: A Critical Analysis of the "Redox Crystallization" Mechanism. *ACS Omega* **2018**, *3*, 1555–1563.

(35) Bullen, C. R.; Mulvaney, P. Nucleation and Growth Kinetics of CdSe Nanocrystals in Octadecene. *Nano Letters* **2004**, *4*, 2303–2307.

(36) Park, K.; Hsiao, M.-s.; Yi, Y.-J.; Izor, S.; Koerner, H.; Jawaid, A.; Vaia, R. A. Highly Concentrated Seed-Mediated Synthesis of Monodispersed Gold Nanorods. *ACS Applied Materials & Interfaces* **2017**, *9*, 26363–26371.

(37) Park, K.; Drummy, L. F.; Wadams, R. C.; Koerner, H.; Nepal, D.; Fabris, L.; Vaia, R. A. Growth Mechanism of Gold Nanorods. *Chemistry of Materials* **2013**, *25*, 555–563.

(38) Rodríguez-Fernández, J.; Pérez-Juste, J.; Mulvaney, P.; Liz-Marzán, L. M. Spatially-Directed Oxidation of Gold Nanoparticles by Au(III)-CTAB Complexes. *The Journal of Physical Chemistry B* **2005**, *109*, 14257–14261.

(39) Gammons, C. H.; Yu, Y.; Williams-Jones, A. The disproportionation of gold(I) chloride complexes at 25 to 200C. *Geochimica et Cosmochimica Acta* **1997**, *61*, 1971–1983.

(40) Gallego, J. H.; Castellano, C.; Calandra, A.; Arvia, A. The electrochemistry of gold in acid aqueous solutions containing chloride ions. *Journal of Electroanalytical Chemistry and Interfacial Electrochemistry* **1975**, *66*, 207–230.

(41) Liu, M.; Guyot-Sionnest, P. Mechanism of Silver(I)-Assisted Growth of Gold Nanorods and Bipyramids. *The Journal of Physical Chemistry B* **2005**, *109*, 22192–22200.

(42) Lofton, C.; Sigmund, W. Mechanisms Controlling Crystal Habits of Gold and Silver Colloids. *Advanced Functional Materials* **2005**, *15*, 1197–1208.

(43) Feigin, L. A.; Svergun, D. I. *Structure Analysis by Small-Angle X-Ray and Neutron Scattering*; Springer, Boston, MA, 1987; Vol. 1.

(44) Kotlarchyk, M.; Chen, S.-H. Analysis of small angle neutron scattering spectra from polydisperse interacting colloids. *Journal of Chemical Phyics* **1983**, *79*, 2461.

(45) Berr, S. Solvent isotope effects on alkytrimethylammonium bromide micelles as a function of alkyl chain length. *Journal of Physical Chemistry* **1987**, *91*, 4760.

(46) Kaya, H. Scattering from cylinders with globular end-caps. *Journal of Applied Crystallography* **2004**, *37*, 223–230.

(47) Onsager, L. The effects of shape on the interaction of colloidal particles. *Annals of the New York Academy of Sciences* **1949**, *51*, 627–659.

(48) Livsey, I. Neutron scattering from concentric cylinders. Intraparticle interference function and radius of gyration. *Journal of the Chemical Society, Faraday Transactions 2* **1987**, *83*, 1445–1452.

(49) Kline, S. R. Reduction and analysis of SANS and USANS data using IGOR Pro. *Journal of Applied Crystallography* **2006**, *39*, 895.